

Valley spin polarization in two-dimensional h -MN ($M = \text{Nb, Ta}$) monolayers: Merger of valleytronics with spintronics

Raihan Ahammed  and Abir De Sarkar ^{*}

Institute of Nano Science and Technology, Knowledge City, Sector 81, Mohali, Punjab-140306, India



(Received 30 October 2021; revised 6 January 2022; accepted 7 January 2022; published 31 January 2022)

The search for new two-dimensional (2D) semiconductors with strong spin-orbit coupling, merging Rashba effect with valley physics, is essential for advancing the emerging fields of spintronics and valleytronics. h -MN ($M = \text{Nb, Ta}$) monolayers are found to host valley physics together with Rashba effect. h -NbN (TaN) monolayers show Zeeman-type valley spin splitting of 32 (112) meV and 130 (406) meV at valence-band and conduction-band edges, respectively, based on density-functional theory calculations. One of the three degenerate valleys around the K/K' point in the first Brillouin zone (BZ) lies fully enclosed within the first BZ. Berry curvature $\sim 50(73) \text{ \AA}^2$ shown by h -NbN (TaN) monolayers is much higher than that in MoS_2 monolayer ($\sim 11 \text{ \AA}^2$), owing to the lower band gap and wave vector magnitude in h -NbN (TaN) monolayers. The Rashba energy splitting and Rashba constant induced by strong spin-orbit coupling (SOC) in h -NbN (TaN) monolayer is found to be 52 (74) meV and 2.9 (4.23) eV \AA respectively, which are amongst the giant Rashba spin-splitting parameters observed so far in 2D materials. The degree of Zeeman-type valley spin splitting and Rashba-type spin splitting is substantially tunable via in-plane biaxial strain and out-of-plane electric field. Higher SOC in h -TaN monolayer relative to h -NbN monolayer caused by the heavier Ta atoms gives rise to a higher Berry curvature, valley-, and Rashba spin splitting in the former as compared to the latter. Valleytronic and spintronic properties in the studied monolayers are found to be superior to that in h - MoS_2 and Janus MoSSe monolayers and are therefore proposed for an effective coupling of spin and valley physics.

DOI: [10.1103/PhysRevB.105.045426](https://doi.org/10.1103/PhysRevB.105.045426)

I. INTRODUCTION

Nowadays, an extra valley degree of freedom (DOF), which is distinct and different from that of electronic charge and spin, has been stimulating intense interest in two-dimensional (2D) materials, offering a novel avenue in device design at the nanoscale [1,2]. The valley DOF occurs from multiply degenerate energy extrema of the valence band (VB) and conduction band (CB) in momentum space. So far, the valley DOF has drawn a great deal of attention in a large number of emergent quantum phenomena, such as valley Hall effect [3] and valley-dependent orbital magnetic moment [4]. Valleytronics is aimed at actively controlling and manipulating the valley DOF in semiconductor devices analogous to the charge DOF in electronics and spin DOF in spintronics [5]. Several materials have been proposed as candidates for valleytronic materials, such as silicon [6], bismuth thin films [7], graphene [8,9], and transition-metal dichalcogenide (TMDC) [2,10] monolayers.

To exploit the valley DOF, it is essential to produce valley polarization via controllable techniques. Thus, various methodologies have been implemented to control valley polarization, such as, optical pumping [11,12], magnetic substrate proximity effect [10,13], and magnetic doping [14]. Charge carriers with suitable combinations of spin and valley

indices are selectively excited by the dynamic process of optical pumping using frequency-specific circular polarizations. Therefore, valley DOF can be utilized to encode information. As the nonequilibrium distribution of carriers of K/K' valley with transient carrier lifetimes [15] will be generated by the dynamical valley polarization upon optical pumping, a rapid transfer of photogenerated carriers is needed to reduce the recombination.

When in-plane electric field is applied, photogenerated electrons and holes by optical excitation at the same K will move along opposite directions under the effect of the Berry curvature, which is nothing but the effective magnetic field in momentum space. But, the Berry curvature vanishes in inversion symmetric or centrosymmetric materials. Hence, broken inversion symmetry is compulsory for valleytronics. The two quantities, Berry curvature [$\Omega_n(k)$] and orbital magnetic moment [$m(k)$] are fundamental quantities in valleytronics [16].

The presence of strong spin-orbit coupling (SOC) in inversion asymmetric materials [17,18] induces Rashba-type spin splitting in the electronic band structure, which can be harnessed effectively in spintronics. The Rashba electronic states reveal unique band dispersion with spin-momentum locking, which can be explained by the Hamiltonian $H_R = \alpha_R \hat{\sigma} \cdot (\hat{\mathbf{k}}_{\parallel} \times \hat{\mathbf{e}}_z)$ as proposed by Rashba *et al.* to describe 2D electron gas [19], where is α_R the Rashba constant, $\hat{\sigma}$ is the vector of the Pauli matrices, $\hat{\mathbf{k}}_{\parallel} = (k_x, k_y, 0)$ is the in-plane momentum of the electrons, and $\hat{\mathbf{e}}_z$ is the out-of-plane unit vector indicating a direction of the local electric field induced

^{*} abirdesarkar@gmail.com

by the asymmetric crystal potential. In heterostructures and at surfaces, the Rashba SOC field plays a crucial role for the electronic states as the structural asymmetry produces an out-of-plane electric field [20]. The Rashba SOC generated linear k -dependent spin splitting of bands enables the control of electron current by steering the spin precession, which is the fundamental principle of action for spin field-effect transistors (SFETs) [21]. An essential factor in constructing such a device requires the channel length $L = \pi \hbar^2 / 2m^* \alpha_R$ over which the spin precesses by π (180°); thus, shorter channel lengths need larger α_R [22].

The Rashba effect in 2D materials has been garnering increasing scientific attention due to its remarkable capability in SFETs [23]. Charge carriers in materials with Rashba SOC experience a momentum-dependent effective magnetic field, a spin-dependent velocity correction resulting from the SOC [24]. These features are particularly attractive for the realization of device concepts [25,26] in which spin polarization is generated from charge current, manipulated by electric field. Rashba effect has been noticed experimentally in semiconductor quantum wells [27,28], polar semiconductors like BiTeI [29], and surfaces of heavy metals [30,31]. Several 2D materials have been predicted theoretically, such as graphene [32], Janus TMDC monolayers [33,34], and Janus transition-metal trichalcogenide monolayers [35] and the MoS₂/Bi (111) heterostructure [36].

The coupling of valley physics arising from spin-valley locking to the Rashba spin-band splitting caused by strong spin-orbit coupling is being increasingly sought after as the key ingredient in the flourishing field of valleytronics and spintronics. Yet, the paucity of 2D materials showing an appreciable spin-valley polarization along with Rashba effect holds back their implementation in next-generation electronics, such as spin valleytronics. Recently, Anand *et al.* [37] theoretically predicted the 2D nanosheets of single-layered niobium nitride, s -NbN, and h -NbN using *ab initio* calculations. Anand *et al.* [37] reported that s -NbN is metallic and preserves the superconducting features of bulk NbN at low temperature, while h -NbN is a semiconductor exhibiting piezoelectric properties. Superconducting properties of high-quality NbN thin films [38,39] have been widely studied experimentally. The dynamical stability of monolayer h -NbN also suggests that it could be synthesized experimentally [37]. Chanana *et al.* [40] demonstrated a strange ferroelectric property in a strained 2D h -NbN monolayer that emanates from its electrons together with phonons, with out-of-plane spontaneous polarization linked with strain and electric field using first-principles density-functional theory (DFT) calculations. They also demonstrate electric field-driven polarization switching in h -NbN at 5% biaxial strain and present a simple model to capture the physics of its strongly coupled electronic and phononic ferroelectricity. Yet, Rashba effect and valley physics were overlooked in h -NbN. In our present work on h -NbN monolayer using first-principles calculations, the presence of time-reversal symmetry and broken inversion symmetry along with Zeeman-type valley and Rashba-type spin splitting is found to bring about a substantial coupling between the spin and valley degrees of freedom, which will facilitate seamless amalgamation of the evolving field of 2D spintronics with valleytronics.

II. COMPUTATIONAL METHODS

In this work, the first-principles calculations have been carried out to study all the electronic properties using DFT [41,42] as implemented in the Vienna *Ab initio* Simulation Package (VASP) [43–46]. The interaction among electrons and nuclei is considered using the plane-wave projector augmented-wave [47,48] method. The exchange-correlation functional within the generalized gradient approximation (GGA) is parametrized by the Perdew-Burke-Ernzerhof (PBE) [49] formalism. We first performed structural relaxation for all materials to get optimized geometry by minimizing the forces on the atoms less than 0.01 eV/Å. A vacuum spacing larger than 15 Å along the z direction has been used to avoid spurious interactions between the adjacent periodic images. These calculations were carried out with a Γ -centered $32 \times 32 \times 1$ Monkhorst-Pack k -point mesh [50] and an energy cutoff of 550 eV. To test the dynamical stability, phonon dispersion calculations have been performed using the density functional perturbation theory [51,52] as implemented in the VASP code along with the PHONOPY [53] package. To plot spin texture, we have considered spin-polarized and noncollinear calculation to incorporate SOC using the VASP package along with the PYPROCAR [54] code. The elastic stiffness coefficients C_{ij} including ionic relaxations have been carried out using the finite-difference method, as implemented in the VASP code.

III. RESULTS AND DISCUSSION

A. Crystal symmetry and electronic property

Monolayer h -NbN has buckled trigonal lattice structure having space group $P3m$ (156) as depicted in Fig. 1(a). Inversion symmetry $[(x, y, z) \rightarrow (-x, -y, -z)]$ is broken in this structure. The optimized lattice constant of the relaxed crystal structure is found to be $|a| = |b| = 3.16$ Å, which is in very close agreement with other theoretical [37] result. The buckling height (Δ) is 0.78 Å. The direct lattice vectors are $\mathbf{a} = 3.16 \mathbf{e}_x$, $\mathbf{b} = -1.58 \mathbf{e}_x + 2.74 \mathbf{e}_y$. The corresponding reciprocal lattice vectors as shown in Fig. 1(i) are $\mathbf{a}^* = 0.32 \mathbf{e}_x + 0.18 \mathbf{e}_y$, $\mathbf{b}^* = 0.36 \mathbf{e}_y$. The high-symmetry k points as indicated in the Brillouin zone are Γ (0,0,0), M (0,0,0.5 b^*), and K (0.333 a^* , 0.333 b^*). A 3D view of the VB and CB about the Fermi level containing the energy extrema (VBM, CBM) is represented in Fig. 1(b). To clearly visualize these two bands, isoenergetic contours are plotted in 2D k space as shown in Figs. 1(c) and 1(d). It is found that the isoenergetic contours near about the valence-band edges are triangularly warped similar to monolayer TMDC [55] such as MoS₂. On the other hand, the isoenergetic contours near about the conduction-band edges are elliptically warped. The electronic band structure with and without SOC, as shown in Fig. 1(e), has been calculated using the GGA-PBE functional. Electronic structure of h -NbN exhibits an indirect band gap of 0.72 eV (without SOC) with VBM and CBM located at wave vectors in between high symmetric $K \rightarrow \Gamma$ k path, which is in excellent agreement with other theoretical report [37] (~ 0.77 eV). The presence of strong SOC and absence of inversion symmetry lifts the spin degeneracy of VB and CB, causing Zeeman-type [see Figs. 1(f) and 1(h)] and

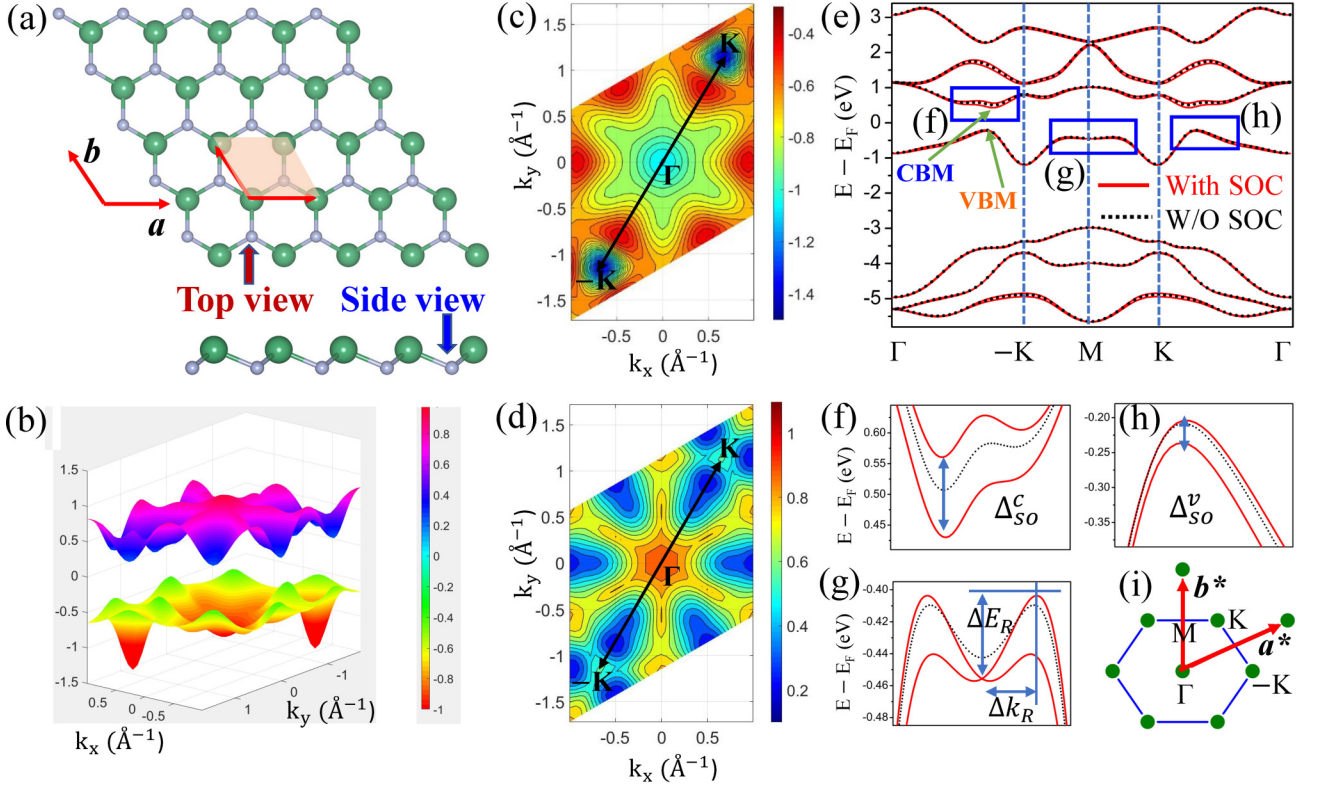


FIG. 1. (a) Top and side view of crystal structure of h -NbN; (b) 3D band structure near Fermi level; (c) energy contours of top VB; (d) energy contours of bottom CB; (e) band structure along high-symmetry k path. (f)–(h) Enlarged view as indicated in (e). Fermi level is set to zero. GGA-PBE functional is used to calculate electronic structure. (i) First Brillouin zone (1BZ) of h -NbN monolayer.

Rashba-type [see Fig. 1(g)] spin splitting, which has been discussed in detail in the following section. The Zeeman-type valley spin splitting (VSS) is found to be 130 meV in the CB (Δ_{SO}^c), whereas VSS in the VB (Δ_{SO}^v) is found to be very small (~ 32 meV) upon introducing the relativistic SOC effect, which is exactly opposite to that of group-VI TMDCs, where small (large) VSS is noticed at CB (VB). The observed Zeeman-type VSS in monolayer h -NbN [$\Delta_{SO}^{c(v)} \sim 130$ (32) meV] is comparable to that of Janus monolayer TMDC MoSSe [56] [$\Delta_{SO}^{c(v)} \sim 13.7$ (170) meV]. The atomic orbital contributions of VB and CB edges involved in the SOC splitting have been investigated as listed in Tables I and II and depicted in orbital projected band structure as shown Fig. S1 in the Supplemental Material (SM) [57]. VB (CB) edge mainly comprises Nb d orbitals with 85.19% (77.91%) contribution and maximum contribution consists of Nb d_{z^2} orbital with 34.20% (40.86%), respectively.

We have also investigated the other 2D monolayers with similar structure of h -NbN monolayer in the family of MX ($M = V, Nb, Ta; X = N, P, As$). Only the monolayers of

VN, NbN, NbP, and TaN show lattice dynamical stability, while the others show very large phonon instability in the out-of-plane flexural acoustic (ZA) phonon mode, as depicted in Fig. S2. Phonon dispersion and dynamical stability of the studied monolayers are discussed in detail in the SM [57] (see, also, Ref. [58] therein). We have studied the electronic properties of the stable structures and compared with NbN monolayer. It is noticed that the nature of band structures of VN and TaN monolayer are similar to NbN monolayer whereas the band structure of NbP monolayer is different from NbN monolayer as shown in Fig. S3. Spin-polarized VSS in both valence and conduction bands is larger (smaller) in h -TaN (h -VN) monolayer relative to h -NbN on account of higher (lower) spin-orbit coupling arising from heavier (lighter) Ta (V) atoms. The value of band gap, SOC splitting in the VB(CB), and Berry curvature are listed in Table III. From Table III and Fig. S4, the trend in band gap is observed as $VN > NbN > TaN$ and $NbP > NbN$; however, the trend in SOC splitting and Berry curvature is opposite to that in band gap as $VN < NbN < TaN$ and $NbP < NbN$. It will be

TABLE I. Orbital contribution to VB edge of h -NbN monolayer.

Orbital	s (%)	p_y (%)	p_z (%)	p_x (%)	d_{xy} (%)	d_{yz} (%)	d_{z^2} (%)	d_{xz} (%)	$d_{x^2-y^2}$ (%)
Nb	1.98	1.07	0.30	0.76	11.14	9.62	34.20	12.06	18.17
N	0.0	4.43	3.82	2.45	0.0	0.0	0.0	0.0	0.0
NbN	1.98	5.50	4.12	3.21	11.14	9.62	34.20	12.06	18.17

TABLE II. Orbital contribution to CB edge of h -NbN monolayer.

Orbital	s (%)	p_y (%)	p_z (%)	p_x (%)	d_{xy} (%)	d_{yz} (%)	d_{z^2} (%)	d_{xz} (%)	$d_{x^2-y^2}$ (%)
Nb	0.36	3.80	1.27	1.45	1.0	25.54	40.86	9.42	1.09
N	0.54	4.17	2.71	7.79	0.0	0.0	0.0	0.0	0.0
NbN	0.90	7.97	3.98	9.24	1.0	25.54	40.86	9.42	1.09

discussed in more detail in the context of Berry curvature and valley physics in a later section.

B. Rashba effect

In monolayer h -NbN, the Zeeman-type spin splitting near the corners of the hexagonal 2D Brillouin zone occurs due to presence of strong SOC together with the breaking of inversion symmetry, $(x, y, z) \rightarrow (-x, -y, -z)$ as well as the Rashba-type spin splitting has been observed around the M point because of the intrinsic out-of-plane electric field induced by mirror symmetry $(x, y, z) \rightarrow (x, y, -z)$ breaking along the z direction. The spin-projected electronic bands in the monolayer h -NbN using GGA-PBE functional with incorporation of SOC, have been shown in Figs. S5(a)–S5(c) and top two valence bands as depicted in Figs. 2(a)–2(c) to study Rashba effect.

The spin-resolved isoenergy contours of the spin-split top two valence bands ($E = -0.5$ eV and $E_F = 0.0$ eV) demonstrate in-plane spin distribution, as displayed in Figs. 2(d)–2(f), which is the signature of the Rashba effect, as observed in the 2D electron systems [19,59]. There is no spin distribution from S_z , while S_x and S_y mostly contribute to the in-plane spin distribution. S_y spin causes Rashba splitting only around $M1$ and $M4$ points along the high-symmetry path Γ - M - K when $k_x = 0$. However, S_x spin causes Rashba splitting around $M2$, $M3$, $M5$, and $M6$ along the high-symmetric path Γ - M - K . It is also clear from the spin texture of top two valence bands as depicted in Fig. S6. We have observed that VB of NbN monolayer at the high-symmetric M point shows the main contribution from Nb p_y (9.72%), Nb $d_{x^2-y^2}$ (15.49%), Nb d_{yz} (60.91%), Nb d_{z^2} (9.52) and N s (3.93%) orbitals as listed in Table S1.

Therefore, Rashba spin splitting occurs due to these orbitals mainly. According to linear Rashba model, the SOC-included spin splitting is described by the well-defined Rashba constant (α_R) as $\alpha_R = \frac{2\Delta E_R}{\Delta k_R}$, where ΔE_R and Δk_R are the Rashba energy splitting and the momentum shift, respectively. The parameters of ΔE_R and Δk_R of h -NbN monolayer are 52.0 meV and 0.0358 \AA^{-1} , respectively; thus, α_R is calculated

TABLE III. Band gap, SOC splitting in VB and CB, and Berry curvature. Band gap has been calculated using Heyd–Scuseria–Ernzerhof (HSE) functional.

2D monolayer	E_g^{HSE} (eV)	$\Delta_{\text{SO}}^{\text{v}}$ (meV)	$\Delta_{\text{SO}}^{\text{c}}$ (meV)	Ω (\AA^2)
VN	0.801	14	35	44
NbN	0.759	32	130	51
NbP	0.803	21	57	25
TaN	0.559	112	406	73

to be 2.905 eV \AA . The value of Rashba constant is comparable to recently predicted 2D Rashba monolayers, such as AlBi (2.77 eV \AA) [60] and BiSb (2.3 eV \AA) [61], and much higher than the conventional semiconducting heterostructure of In-GaAs/InAlAs ($\alpha_R \sim 0.07 \text{ eV \AA}$) [27], metallic surface state of Au (111) surface ($\alpha_R \sim 0.33 \text{ eV \AA}$) [62] and Bi (111) surface ($\alpha_R \sim 0.55 \text{ eV \AA}$) [63], monolayer Janus MoSSe ($\alpha_R \sim 0.077 \text{ eV \AA}$) [34], and Janus WSeTe ($\alpha_R \sim 0.514 \text{ eV \AA}$) [34]. Modulation of Rashba parameters has been investigated by applying in-plane biaxial compressive and tensile strain up to 5%. It has been found that Rashba parameter α_R is enhanced to 2.944 eV \AA at 2.5% tensile strain. In general, a large Rashba parameter implies significant SOC, which is desirable for suppressing the spin relaxation, controlling the spin precession, and the system's stability and robustness against all forms of spin-independent scattering [24,64]. As a consequence, structures with large Rashba-type splitting are sought after. We have also studied the changes in Rashba properties upon changing the cation and anion elements, as depicted in Table IV and Fig. S7. The trend in Rashba parameter is observed as $\text{VN} < \text{NbN} < \text{TaP}$ and $\text{NbP} < \text{NbN}$. TaN monolayer shows highest energy offset ($\Delta E_R \sim 74 \text{ meV}$) and Rashba parameter ($\alpha_R \sim 4.229 \text{ eV \AA}$), as the spin-orbit coupling strength is larger in heavier atoms. A large Rashba parameter indicates that monolayer h -NbN and h -TaP could be realized as a promising candidate in spin field-effect transistors.

Several possible descriptors have been taken into consideration to deduce a relationship with Rashba parameters of different monolayers such as electronegativity, ionization energy, Bader charges, Born effective charges, and out-of-plane electric field asymmetry as depicted in Figs. 3(a)–3(f). Asymmetry in crystal potential as well as electric field perpendicular to the 2D plane as shown in Figs. S8 and S9 is also responsible for Rashba effect. The out-of-plane electric field at the specific atom site is calculated from electrostatic potential using the central difference method ($E = -\frac{dV}{dz}$). The strength of electric field asymmetry is evaluated as $|\tilde{E}| = |\tilde{E}_M - \tilde{E}_X|$. It is observed that $|\tilde{E}|$ does not correlate well with α_R as depicted in Fig. 3(d). Bader charges of individual atom as calculated using Bader code [65] are also not found to be a good descriptor [Fig. 3(c)]. Only Z_{zz}^* is found to correlate well with α_R . Out-of-plane Born effective charges on each atom

TABLE IV. Rashba parameters.

2D monolayer	ΔE_R (eV)	Δk_R (\AA^{-1})	α_R (eV \AA)
VN	0.030	0.0376	1.618
NbN	0.052	0.0358	2.905
NbP	0.002	0.0057	0.548
TaN	0.074	0.0350	4.229

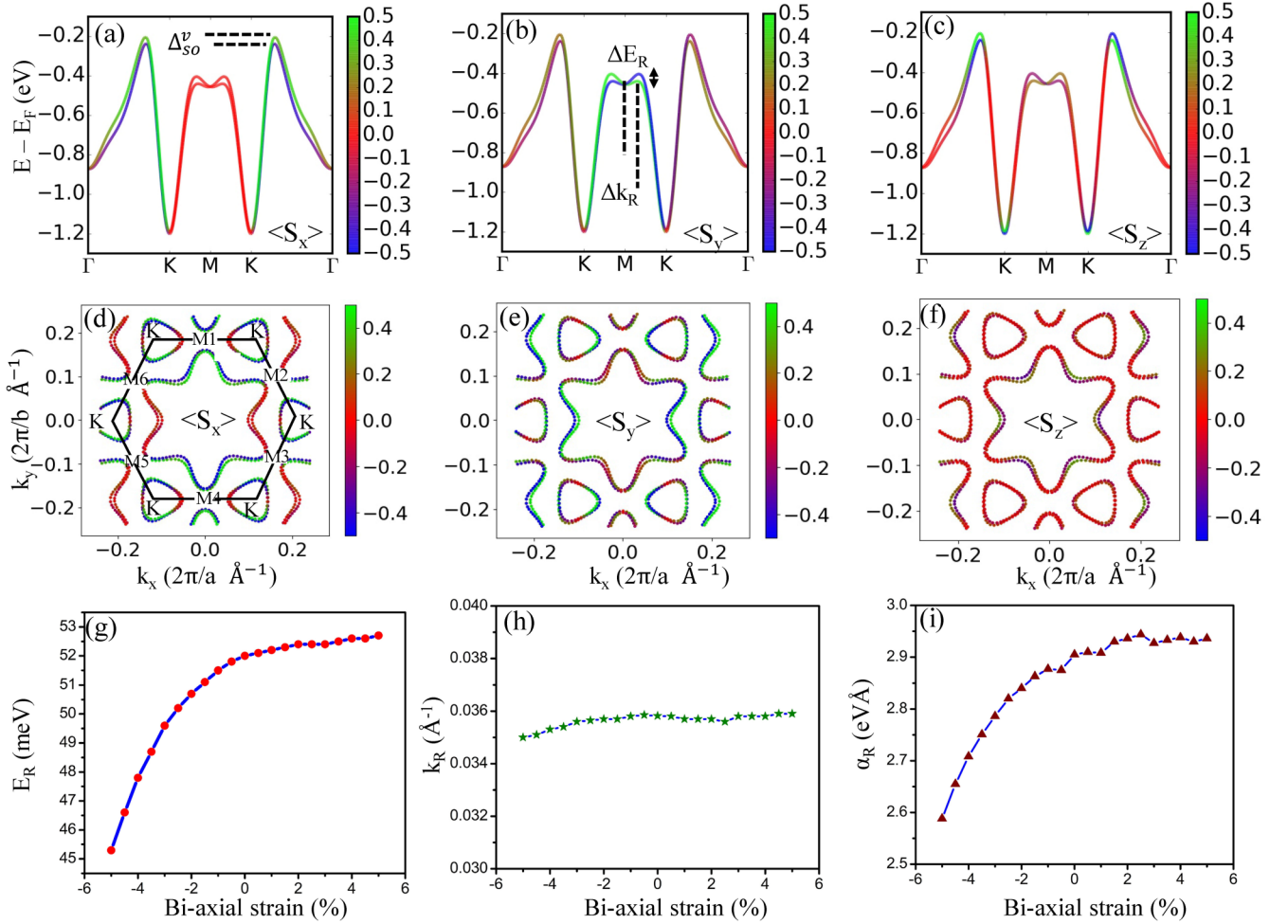


FIG. 2. Spin projected top two valence bands, i.e., (a) S_x , (b) S_y , and (c) S_z in h -NbN. Corresponding contour plot (d)–(f) at $E = 0.5$ eV, $E_F = 0$ eV; color map represents the expectation value of corresponding spin projection. Modulation of (g) energy offset E_R , (h) momentum offset k_R , and (i) Rashba parameter α_R , with biaxial strain.

in these monolayers are found to be a proper descriptor to gauge strength of Rashba effect. Born effective charges (Z_{ij}^* , a tensor) on the ions is different from the formal static charge and corresponds to the amount of charge that effectively contributes to the polarization during external perturbation such as ionic displacement. The dynamical Born effective charge is defined as $Z_{ij}^* = (\Omega/e) (\partial P_i / \partial u_j) = (1/e) (\partial F_i / \partial E_j)$; $i, j = x, y$, and z , Ω is the unit-cell volume, u is the strain, E is the electric field, and F is the Hellmann-Feynman forces. The scalar charge on each atom Z^* is given by $\text{Tr}(Z_{ij}^*)$. Microscopically, Born effective charge (Z^*) of the atoms is a sum of static charge [$Z(u)$] and anomalous contributions, $Z^*(u) = Z(u) + u \partial Z(u) / \partial u$, u is the interatomic distance. The Born effective charge Z^* is a fundamental quantity in the study of lattice dynamics, because it governs the amplitude of the long-range Coulomb interaction between nuclei, and the splitting between longitudinal optic (LO) and transverse optic (TO) phonon modes. The dynamical charge measures the macroscopic current flowing across the sample while the ions are adiabatically displaced. Such currents are responsible for building up spontaneous polarization.

The collective displacements of atoms participating in interatomic chemical bonds, hybridization of orbitals, and

charge exchange depends on the Z^* of atoms in the monolayers. Qualitatively, chemical bonding is understood to be influenced by the polarizability and dielectric constants of the materials, which are related to Z^* . Although the total Z^* is not a good descriptor for Rashba parameter of the studied material, only the zz component of Z^* (Z_{zz}^*) shows a good trend as depicted in Figs. 3(e) and 3(f).

C. Valley physics of h -NbN monolayer

On account of the hexagonal honeycomb lattice structure and broken in-plane inversion symmetry in h -NbN monolayer, it shows valley physics or valleytronic properties, i.e., opposite spins are locked to the K and K' valleys at the band edges. When h -NbN will be supported on a substrate to realize its practical applications, the lattice mismatch between the underlying support and h -NbN monolayer can induce a strain in h -NbN. Besides, even in van der Waals heterostructures, incommensurate lattices can bring about interfacial strain. Strain is therefore unavoidable in ultrathin, flexible 2D nanosheets. Therefore, it is instructive to investigate the effect of strain on various properties in 2D materials, including valleytronics. The role of strain has been addressed in this study.

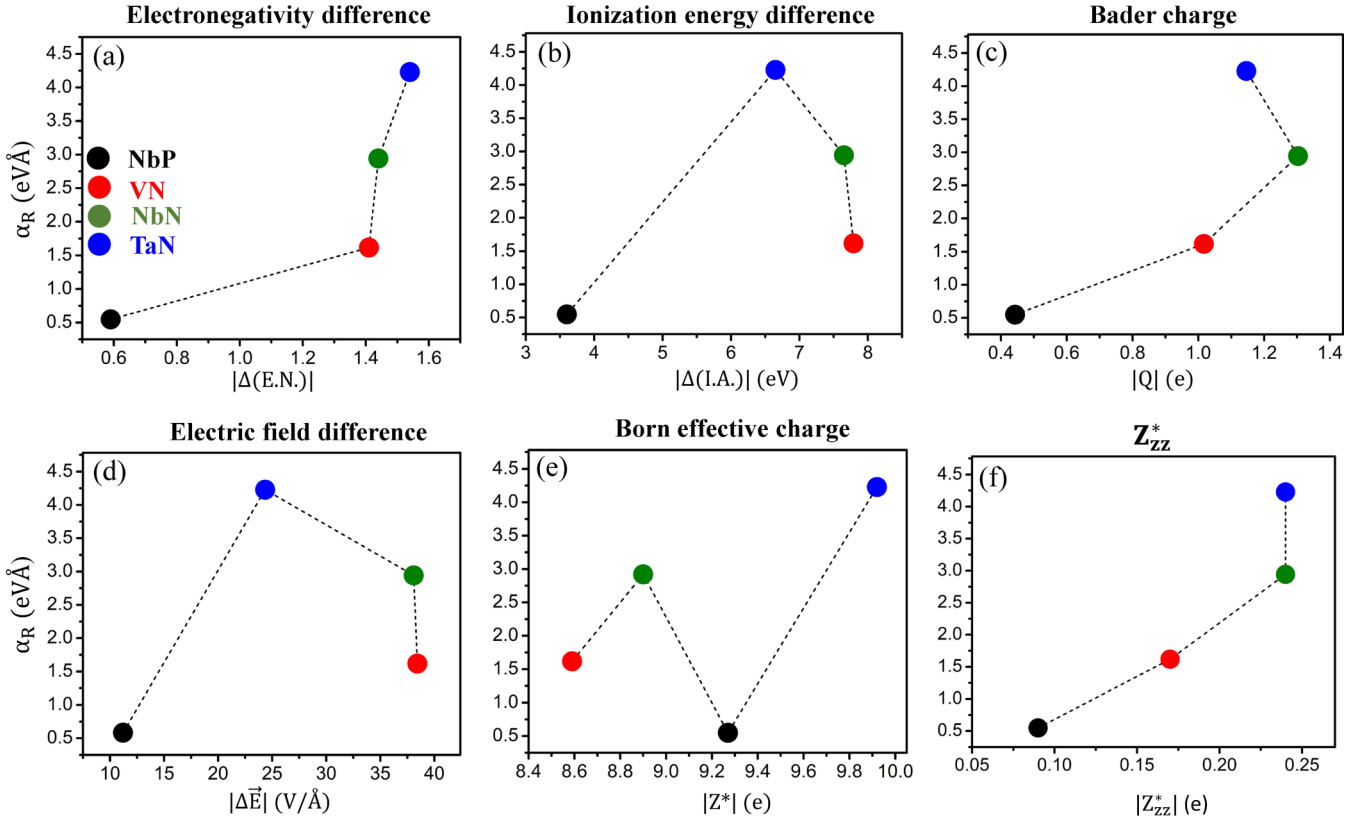


FIG. 3. The Rashba parameter plotted as a function of different material descriptor: (a) electronegativity difference; (b) ionization energy difference; (c) Bader charges; (d) asymmetry in electric field; (e) Born effective charge (Z^*), and (f) zz component of Z^* .

Biaxial tensile and compressive strain in a dilation deformation range of 5% have been applied on monolayer h -NbN to investigate the evolution in the band edges with strain as shown in Figs. 4(a)–4(c). With the application of tensile (compressive) biaxial strain, band gap is decreasing (increasing) while the Zeeman-type VSS Δ_{SO}^v and Δ_{SO}^c are found to be almost invariant as displayed in Figs. S10(a) and S10(b). A robust strain-valley coupling between mechanical strain and low-energy Bloch bands around the band edges on either side of the Fermi level has been observed, where an applied elastic deformation by biaxial strain substantially drifts the CB and VB edges (i.e., valleys and hills) far away from K/K' -points in the momentum space, as depicted in Figs. 4(b) and 4(c). The isoenergetic contours of highest occupied valence band and lowest unoccupied conduction band near about the band edges have been depicted in Figs. 4(d)–4(i) to shed further light into valley drift. Unlike graphene, the isoenergy contours of the band edges in a monolayer h -NbN are not isotropic in the close proximity of the $K1$ point and an elliptical warping effect of energy bands can be seen in the isoenergy lines around the $K1$ point.

As shown in Figs. 4(g)–4(i), the lowermost spin-split conduction-band edge ($CB1$) drifts off the $K1$ point at a rate $(\Delta k/\text{tensile strain}) \sim 1.52 \times 10^{-3} \text{ \AA}^{-1}/1\%$ when biaxial tensile strain is applied, while it drifts off along the opposite direction at a rate $(\Delta k/\text{compressive strain}) \sim 2.57 \times 10^{-3} \text{ \AA}^{-1}/1\%$ when biaxial compressive strain is applied. We find the energy valley drift in spin-split $CB1$ to be higher ($>1.6\times$) upon compressive strain than the corresponding drift due to tensile

strain which is attributable to the different kinds of variation in elastic constants, Young's modulus (Y), and Poisson ratio (ν) with tensile and compressive strain [see Figs. 6(a) and 6(b)]. A similar valley drift for the uppermost spin-split valence-band edge ($VB1$) is observed. The valence-band edge drifts away from the $K1$ point at a rate $\sim 1.80 \times 10^{-3} \text{ \AA}^{-1}/1\%$ when biaxial tensile strain is applied, while it drifts off along the opposite direction at a rate $\sim 2.88 \times 10^{-3} \text{ \AA}^{-1}/1\%$ when compressive strain is applied. The valley drift of holes is found to be higher than that of the electrons on account of higher in-plane d -orbital contribution of VB edge [d_{xy} (11.14%), $d_{x^2-y^2}$ (18.17%)] than that of CB edge [d_{xy} (1.0%), $d_{x^2-y^2}$ (1.09%)], which is clearly observed in Tables I and II. The plane-average squared wave functions ($|\psi|^2$) have been projected along the direction perpendicular to the basal plane of h -NbN monolayer for pristine and strained system as depicted in Figs. 5(a) and 5(b). VB edge is found to be more delocalized than the CB edge, which is also evident from the corresponding charge-density distribution originating from orbital wave functions of the specific band edges, as shown in Figs. 5(c)–5(h). Under compressive strain, the probability amplitude for both VB and CB edges increases, while for tensile strain it decreases.

A similar valley-drift response has been noticed in graphene [66] on account of its two-dimensional hexagonal structure. Although the drift is much enhanced in monolayer h -NbN, however it is lower than that in monolayer MoS_2 . Per percent of strain, the valley-drift response is found to be nearly $0.6(7.5)10^{-3} \text{ \AA}^{-1}/1\%$ in graphene (MoS_2) [66,67]. The valley

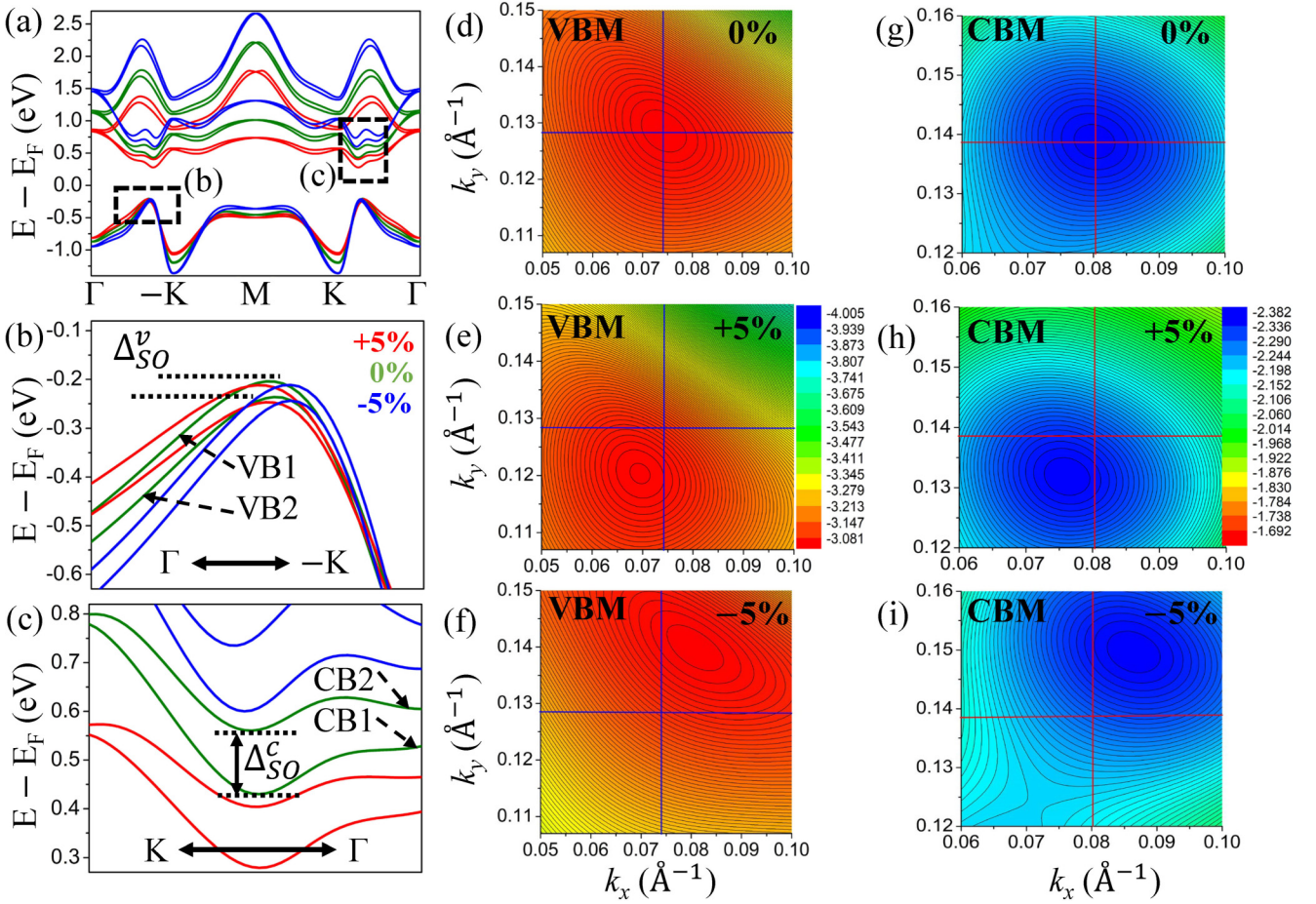


FIG. 4. (a) Modulation of band structure of monolayer h -NbN with 5% compressive and tensile strain using GGA-PBE functional along with SOC. (b), (c) Enlarged view of VB and CB as indicated (a). Isoenergy contours of low-energy valence bands of (d) 0% strain, (e) +5%, and (f) -5% biaxial strain, respectively. Isoenergy contours of low-energy conduction bands of (g) 0% strain, (h) +5%, and (i) -5% biaxial strain respectively.

drifts have immediate impacts on valleytronics performances, which is also applicable to the strong coupling between the spin and valley degrees of freedom [67]. As the valley degree of freedom is used to characterize the charge carriers [68], large valley shifts will induce decoherence and thus limit the performance of devices. In monolayer h -NbN, lesser valley shift is observed under tensile/compressive strain for both VBM and CBM than the monolayer MoS₂, which originates from its lower Young's modulus (~ 94.7 N/m) than that in MoS₂ (~ 124.1 N/m) monolayer.

The elastic deformation of materials plays a fundamental role in the electronic properties. Therefore, in modern electronics applications, it is crucial to get an in-depth understanding of elastic properties of the studied material. The elastic stiffness constants (C_{ij}) have been calculated with the forward difference method using the GGA-PBE functional as implemented in VASP and all the mechanical properties such as Young's modulus (Y), Poisson ratio (ν), critical buckling strain (ϵ_c), and intrinsic strength (σ_{int}) have been systematically investigated.

The 2D layer modulus, which indicates the resistance of a nanosheet to stretching, is defined by [16,69] $\gamma^{2D} = \frac{1}{2}[C_{11} + C_{12}]$ while Young's modulus (Y) = $\frac{C_{11} - C_{12}}{C_{11}}$, Poisson ratio (ν) = C_{12}/C_{11} , shear modulus (G) = C_{66} . Moreover, in-

trinsic strength (σ_{int}) and bending modulus (D) of a nanosheet can be evaluated using $\sigma_{\text{int}} \sim \frac{\gamma}{9}$, $D = \frac{\gamma \Delta^2}{12(1-\nu^2)}$, where Δ is the thickness of the nanosheet ($\Delta = 0.78$ Å). The elastic constants determined for the monolayer satisfy Born-Huang stability criteria and other mechanical properties are listed in Table V.

Born-Huang stability criteria:

$$C_{11} > |C_{12}|, C_{22} > 0, C_{66} > 0, C_{11}C_{22} - C_{12}^2 > 0.$$

The critical buckling strain (ϵ_c) of a 2D material can be evaluated using $\epsilon_c = -\frac{4\pi^2 D}{\gamma L^2}$, where L is the length of the 2D nanosheet in the unit of Å. For the same length L (in Å), the critical buckling strain for the h -NbN are found to be $\epsilon_c = -\frac{2.11}{L^2}$, which is comparable to graphene ($-\frac{2.2}{L^2}$) [69]. Young's modulus (~ 94.72 N/m) is found to be smaller than other 2D nanosheets such as graphene (~ 347.1 N/m) [69] and MoS₂ (~ 124.1 N/m) [69], which suggests that h -NbN monolayer will be more flexible than these monolayers. In Figs. 6(a) and 6(b), modulation of the elastic stiffness constants (C_{11} , C_{12}), Young's modulus (Y), and Poisson's ratio (ν) via biaxial tensile and compressive strain have been investigated and the nature of variation in these elastic properties corroborates well the valley-drift response to strain, respectively.

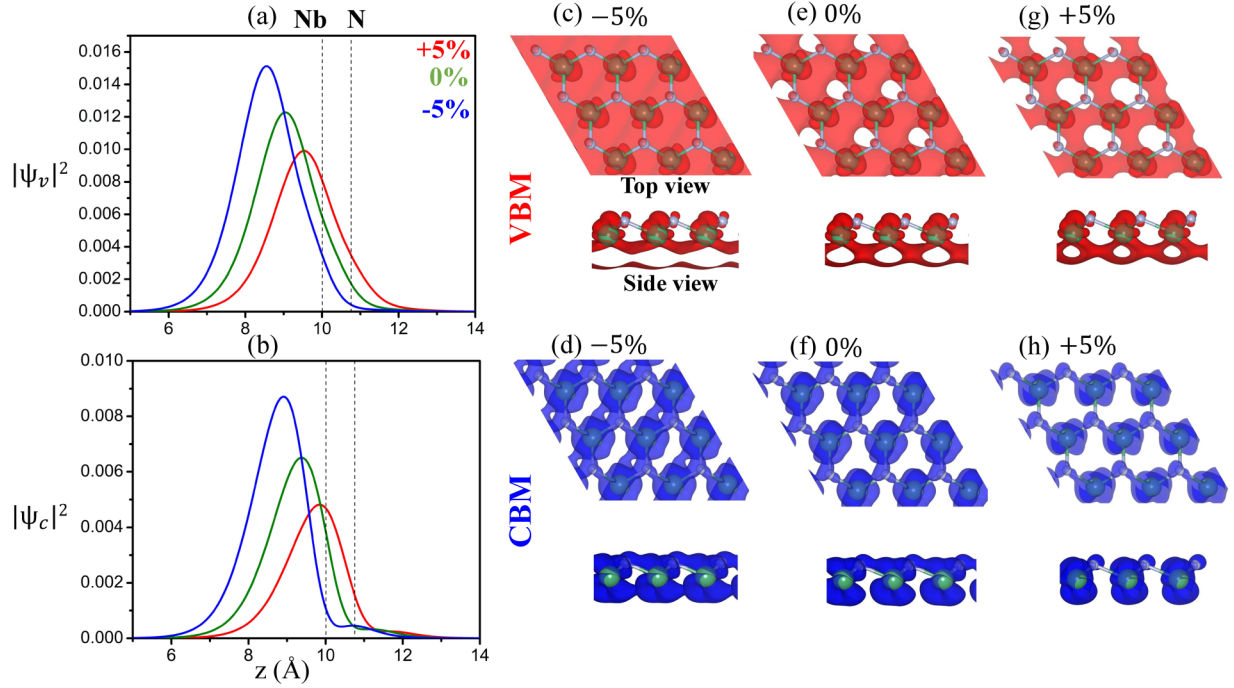


FIG. 5. Spatial profile of Bloch wave functions for (a) VB- and (b) CB edge states projected along the direction perpendicular to the basal plane of h -NbN monolayer. The atomic positions have been marked therein with dashed vertical lines on Nb-N in the pristine (0%) system. Charge density of electronic states at the edges of VB hills and CB valleys for a 5% compressive strained (c), (d); a strain-free (e), (f); and a 5% tensile strained h -NbN monolayer (g), (h). Isosurface value is set to $0.01 \text{ eV}/\text{\AA}^3$.

D. Berry curvature modulation in h -NbN monolayer

It should be emphasized that the velocity of the carriers with a nonzero Berry curvature can be represented as $\hbar \mathbf{v}_n(\mathbf{k}) = \mathbf{v}_g - \mathbf{v}_\perp$, where \mathbf{v}_g indicates the common group velocity, \mathbf{v}_\perp denotes the transverse velocity, while $\mathbf{v}_n(\mathbf{k})$ is derivable from the solution of the Boltzmann transport equation. Group velocity is defined as $\mathbf{v}_g(\mathbf{k}) = \nabla_{\mathbf{k}} \varepsilon_n(\mathbf{k})$, where ε_n corresponds to the energy of the n th Bloch band. In addition, nonzero Berry curvature leads to an anomalous velocity, that is, the transverse velocity \mathbf{v}_\perp , which is indispensable for the valley Hall effect. The transverse velocity can be described as $\mathbf{v}_\perp = -\frac{e}{\hbar} \mathbf{E} \times \boldsymbol{\Omega}(\mathbf{k})$, where \mathbf{E} is the in-plane electric field and $\boldsymbol{\Omega}(\mathbf{k})$ is the out-of-plane Berry curvature [70]. Actually, large $\boldsymbol{\Omega}(\mathbf{k})$ can amplify the transverse velocity, and the excited carriers moving in the direction perpendicular to \mathbf{E} can therefore

be transported faster and their recombination can be reduced [64].

The Berry curvature $\Omega_n(k)$ of band n at the \mathbf{k} point is calculated from the first-principles wave function, using the Kubo formula [71,72] given by

$$\Omega_n(k) = -2\text{Im} \sum_{m \neq n} \frac{\langle \psi_{nk} | \hat{v}_x | \psi_{mk} \rangle \langle \psi_{mk} | \hat{v}_y | \psi_{nk} \rangle}{(E_{nk} - E_{mk})^2}, \quad (1)$$

where $\hat{v}_{x,y}$ are the velocity operators and the summation are over all the occupied states. $\Omega_n(-k) = -\Omega_n(k)$ as a consequence of time-reversal symmetry.

The k, p Hamiltonian [2] to describe low-energy electronic states of hexagonal system in the vicinity of band edges

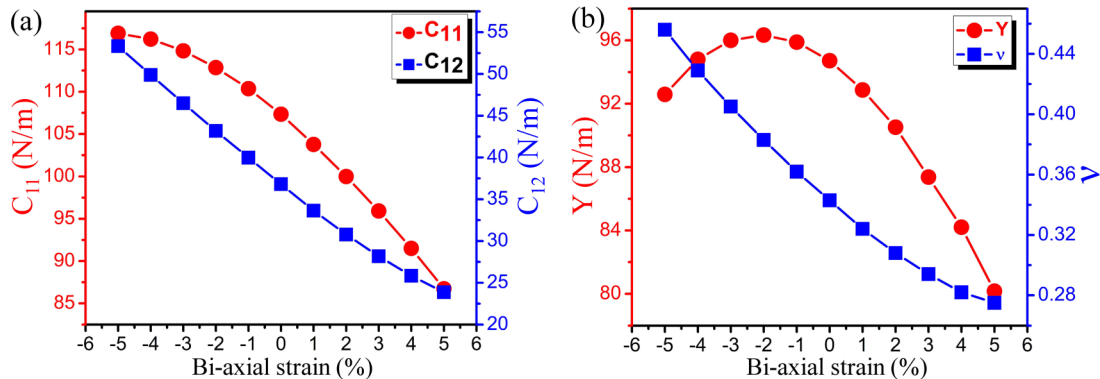


FIG. 6. Variation in (a) elastic stiffness constants C_{11} and C_{12} . Variation in (b) Young's modulus Y and Poisson's ratio ν with biaxial strain.

TABLE V. The calculated mechanical stiffness constants C_{ij} , layer modulus (γ^{2D}), Young's modulus (Y), Poisson's ratio (ν), intrinsic strength (σ_{int}), and bending modulus (D).

System	C_{11} (N/m)	C_{12} (N/m)	C_{66} (N/m)	γ^{2D} (N/m)	Y (N/m)	ν	σ_{int} (N/m)	D (eV)
h -NbN	107.342	36.817	35.263	72.079	94.715	0.343	10.524	5.059

including spin-orbit coupling is given by

$$H = at(\tau k_x \sigma_x + k_y \sigma_y) + \frac{\Delta}{2} \sigma_z - \lambda \tau \frac{\sigma_z - 1}{2} S_z, \quad (2)$$

where a is the lattice spacing, t is the nearest-neighbor hopping integral, $\tau = \pm 1$ is the valley index, $\sigma_{x/y/z}$ is the Pauli matrix spanned by the conduction and valence states, S_z is the Pauli matrix for a spin, Δ is the band gap, and λ is spin splitting. The $k.p$ model is generally exploited in studying valleytronics in 2D materials [16,73,74]. The Berry curvature in the valence band is given by

$$\Omega_v(k) = \tau \frac{2a^2 t^2 \Delta}{(4a^2 t^2 k^2 + \Delta^2)^{3/2}}. \quad (3)$$

Berry curvature in the conduction band is equal in magnitude but opposite in sign to that of the valence band, i.e., $\Omega_c(k) = -\Omega_v(k)$.

In the process of direct intervalley optical excitations through a circularly polarized light, only the orbital part of Bloch wave functions near the K/K' valleys of hexagonal monolayer (ML) TMDC couple to the optical field, although the spin component of carriers remains unchanged during this process. In ML-MoS₂, the electron/hole bands around K/K' are energetically degenerate. But, the opposite nature of Berry curvature distributions, $\Omega(k)$ near the K/K' valleys helps to distinguish the valley carriers. The strength of Berry curvature distribution of valley carriers in ML-MoS₂ can be altered significantly by tuning the onsite electronic energy and orbital occupation factor of a given Bloch state with application of tensile or compressive strain. Similar behavior of Berry curvature can be found in the monolayer h -NbN. We have investigated the effect of biaxial strain on the $\Omega(k)$ of electron/hole bands near $K1$ points lying along the high-symmetry Γ - K path. Unlike ML-MoS₂, in monolayer h -NbN the low-energy valleys are not exactly around the high-symmetry K point. Due to threefold rotational C_3 symmetry, three similar and degenerate valleys of same Berry curvature around the high-symmetry K point have been observed which is a very rare occurrence, thereby exhibiting great possibilities for spin-valley physics in this material. The Berry curvatures of a pristine (0% strain) and strained monolayer h -NbN for all the occupied bands below the Fermi energy along the high-symmetry line Γ - K - M - K - Γ has been shown in Fig. 7(b). The presence of strong spin-orbit interaction along with time-reversal symmetry and absence of lattice inversion symmetry allows charge carriers of alternate valleys to exhibit opposite Berry curvatures as well as opposite spin polarization, where the Berry curvature, $\Omega(k)$, is mostly confined around the $K1/K2$ valleys and found to be highest at both the $K1$ and $K2$ valleys in the BZ with opposite sign. While away from $K1/K2$, $\Omega(k)$ decays rapidly to almost zero at the K point. In between, K - M path, a small peak arises and vanishes at the M point.

Equation (3) clearly shows that the Berry curvature varies inversely as the magnitude of wave vector (k) and band gap (Δ). As the wave vector ($\sim 0.147 \text{ \AA}^{-1}$) and band gap ($\sim 0.72 \text{ eV}$) in h -NbN monolayer are smaller than those in MoS₂ monolayer ($\sim 0.210 \text{ \AA}^{-1}$, 1.69 eV) [75], Berry curvature in h -NbN monolayer ($\sim 51 \text{ \AA}^2$) is found to be more than $4\times$ than the MoS₂ monolayer ($\sim 11 \text{ \AA}^2$) [75]. Recently, Duo *et al.* [76] theoretically predicted strong spin-valley coupling in 2D monolayers of MN_2X_2 ($M = \text{Mo, W}$; $X = \text{F, H}$) and reported Berry curvature $\sim 19.3 \text{ \AA}^2$ in monolayer WN_2F_2 . To facilitate a reasonable functioning of the valleytronic device, it is essential to understand the physical mechanism underlying tunable Berry curvature in order to regulate the transverse transport velocity of carriers. In contrast to the previous strategies adopted to realize tunable Berry curvature, such as constructing heterostructures of distinct 2D materials [20] and applying uniaxial strain (to such as monolayer MoS₂) [77], we have shown that biaxial strain engineering could also effectively tune the magnitude of the Berry curvature. $\Omega(\mathbf{k})$ can be enhanced to the value of 60 \AA^2 by applying 5% biaxial tensile strain as depicted in Fig. 7(b). Application of biaxial strain reduces the band gap and the magnitude of the wave vector and hence, enhances the Berry curvature. Similarly, Wang *et al.* [64] investigated tunable Berry curvature in Janus TiXY ($X \neq Y$, $X/Y = \text{Cl, Br, I}$) monolayers and showed that

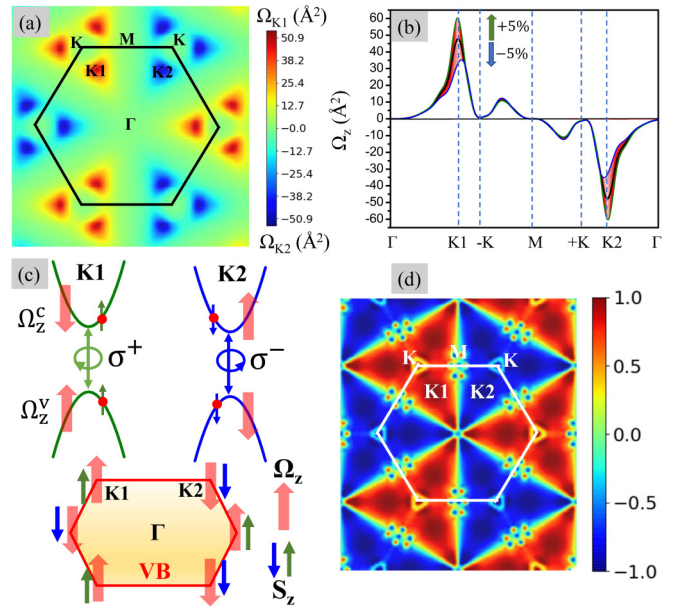


FIG. 7. (a) Contour map of Berry curvature distribution, $\Omega(k)$ of h -NbN monolayer in 2D k space over all occupied Bloch bands of in units of Å^2 . (b) Modulation of Berry curvature distribution along high-symmetry k -line Γ - K - M - K - Γ with application of biaxial strain; (c) schematic of valley-selective excitation; and (d) circular dichroism polarization, $\eta(k)$.

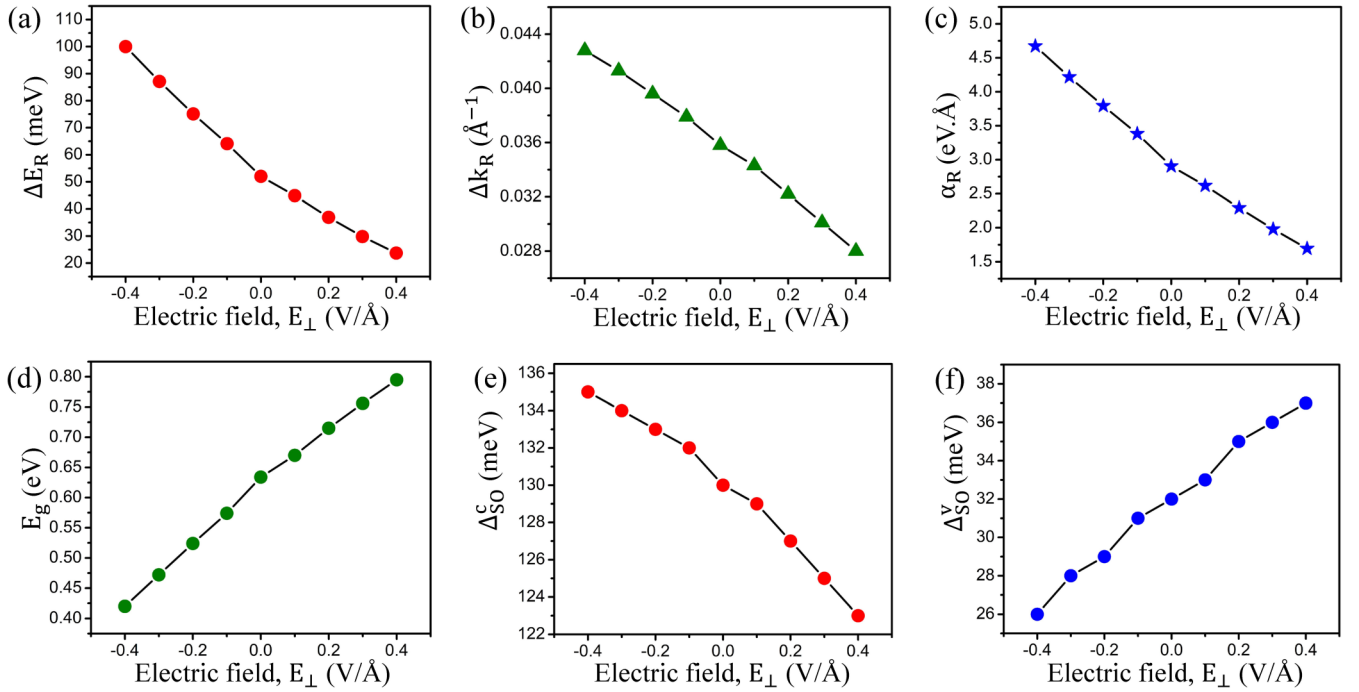


FIG. 8. Vertical electric field modulation of (a) Rashba energy offset (ΔE_R); (b) momentum offset (Δk_R); (c) Rashba constant (α_R); (d) band gap (E_g); (e) CB SOC splitting (ΔS_0^c); and (f) VB SOC splitting (ΔS_0^v) in h -NbN monolayer.

Berry curvature, $\Omega(\mathbf{k})$ of monolayer TiBrI can be enhanced to the value of 37.4 \AA^2 by applying 2.5% biaxial tensile strain from 29.7 \AA^2 in pristine structure.

Similar to valley-contrasting Berry curvature $\Omega_n(k)$ at the $K1$ and $K2$ points in the BZ, it is expected to have valley-contrasted circular dichroism $\eta(k)$ as depicted in Fig. 7(d) allowing selective excitation in the two valleys by photons with different optical circular helicity permitting valley-dependent manipulation. Li *et al.* [78] have investigated valley-dependent properties of monolayer MSi_2N_4 ($M = \text{Mo, W}$) and shown that valley fermions manifest spin-valley coupling and valley-selective optical dichroism. The Berry curvature $\Omega(k)$ and optical circular dichroism $\eta(k)$ are related by

$$\eta(k) = \frac{\Omega_n(k)\hat{z}}{\mu_B^*(k)} \frac{e}{2\hbar} \Delta(k), \quad (4)$$

where $\mu_B^* = e\hbar/2m^*$ and $\Delta(k) = [\varepsilon_c(k) - \varepsilon_v(k)]$ is the transition energy, or band gap at k .

The optical polarization is defined as the difference between the absorption of the right- and left-handed circularly polarized lights [RHCP (σ^+)/LHCP (σ^-)], normalized by total absorption at each point in k space, evaluated between the top of the valence bands (v) and the bottom of conduction bands (c). The k -resolved degree of optical polarization between the top of valence bands and bottom of conduction bands is called circular dichroism and it is calculated as $\eta(k) = \frac{|P_+^{cv}|^2 - |P_-^{cv}|^2}{|P_+^{cv}|^2 + |P_-^{cv}|^2}$, where the transition matrix element is $P_{\pm}^{cv}(\mathbf{k}) = \frac{1}{\sqrt{2}} [P_x^{cv}(\mathbf{k}) \pm iP_y^{cv}(\mathbf{k})]$.

The interband matrix elements, $P^{cv}(\mathbf{k}) = \langle \psi_{c\mathbf{k}} | -i\hbar\nabla | \psi_{v\mathbf{k}} \rangle$, are evaluated from DFT calculations using GGA functional. Circular dichroism polarization due

to the direct interband transition from the vicinity of the valence-band edge to the vicinity of the conduction band edge can be clearly seen in Fig. 7(d). At the energetic minima at the $K1$ and $K2$ points, full selectivity occurs when $\eta(k) = \tau$. The interband transitions at the $K1$ valley ($\tau = +1$) only couples to RHCP (σ^+), whereas LHCP (σ^-) is used to excite the carriers at the $K2$ valley ($\tau = -1$), as pictorially shown in Fig. 7(c). A right-handed (left-handed) circularly polarized photon can be selectively absorbed around the $K1(K2)$ valley, while a left-handed (right-handed) one is totally forbidden. Consequently, the nonequilibrium distribution of charge carriers in two inequivalent valleys can be produced by selective optical pumping through circularly polarized light, which is essential for realizing valley Hall effects [79].

E. Response to vertical electric field

As electric field control of Rashba SOC is of great significance in semiconductor spintronics, the application of an external electric field to the h -NbN monolayer has also been studied. In this section, a vertical electric field varying from -0.4 to $+0.4$ V/Å has been applied, and its response to Rashba splitting has been investigated. Rashba spin splitting and valley Zeeman splitting have been observed, as shown in Figs. 8(a)–8(f), which shows that the Rashba constant α_R is linearly dependent on the strength of the electric field. Such a linear relationship between the electric field and the Rashba SOC strength will help a precise control of the spin precession in the spin field-effect transistor. Under the application of a positive electric field, the values of the Rashba parameters are lowered, while the negative electric field increases the Rashba parameters. The value of α_R is found to be regulated from 1.693 to 4.673 eV.Å. Recently, similar modulation of Rashba

constant via vertical electric field was reported in ZnTe monolayer, where it rises from 0.9 to 1.35 eV Å [80]. Electric field response of CB SOC splitting ($\Delta_{\text{SO}}^{\text{c}}$) and VB SOC splitting is found to be of opposite nature. With the application of positive (negative) electric field, $\Delta_{\text{SO}}^{\text{c}}$ decreases (increases), while $\Delta_{\text{SO}}^{\text{v}}$ increases (decreases). $\Delta_{\text{SO}}^{\text{c}}$ ($\Delta_{\text{SO}}^{\text{v}}$) can be modulated from 123 (26) to 135 (37) meV. Band gap is also linearly changed from 0.420 to 0.795 eV. Such great tunability in the Rashba and valley properties under the vertical electric field is very useful in designing spintronic and valleytronic devices.

IV. CONCLUSION

In summary, *h*-NbN and TaN monolayers have been demonstrated to be promising 2D valleytronic and spintronic materials on account of large Zeeman-type valley spin splitting and Rashba-type spin splitting. Monolayer *h*-NbN (TaN) shows Zeeman-type VSS of 32 (112) meV and 130 (406) meV in VB and CB, respectively. At the same time, it exhibits large Berry curvature $\sim 50(73) \text{ \AA}^2$, which is more than 4 (6) \times of monolayer MoS₂ ($\sim 11 \text{ \AA}^2$). Inclusion of spin-orbit coupling yields the giant Rashba-type spin splitting in the VB near the Fermi level. The Rashba energy and Rashba splitting constant of monolayer *h*-NbN (TaN) are found to be 52 (74) meV and

2.90 (4.23) eV Å, respectively, which are competitive with the giant Rashba spin-splitting parameters realized so far in 2D materials. The strength of Zeeman-type valley spin splitting and Rashba-type spin splitting is found to be substantially tweakable upon employing in-plane biaxial strain and out-of-plane electric field to the *h*-NbN monolayer, owing to the mechanical flexibility in this 2D material. Our results suggest that this theoretically predicted 2D material could serve as an ideal platform for studying valley physics, Rashba physics, and for the integration of valleytronics with the spintronics. The true indicator of strength of Rashba constants is found to be the dynamical Born effective charge (Z_{zz}^*) along the out-of-plane *z* direction.

ACKNOWLEDGMENTS

We acknowledge with gratitude the infrastructural *cum* fellowship support given by the Institute of Nano Science and Technology (INST), Mohali, India. The supercomputing facilities provided by INST, Mohali (in-house), and C-DAC, Pune, India, on PARAM-YUVA-II, Pune, and PARAM-SHIVAY at IIT, Varanasi, under the National Supercomputing Mission, Government of India are gratefully acknowledged.

-
- [1] D. Xiao, W. Yao, and Q. Niu, *Phys. Rev. Lett.* **99**, 236809 (2007).
- [2] D. Xiao, G.-B. Liu, W. Feng, X. Xu, and W. Yao, *Phys. Rev. Lett.* **108**, 196802 (2012).
- [3] K. F. Mak, K. L. McGill, J. Park, and P. L. McEuen, *Science* **344**, 1489 (2014).
- [4] J. Qi, X. Li, Q. Niu, and J. Feng, *Phys. Rev. B* **92**, 121403(R) (2015).
- [5] J. R. Schaibley, H. Yu, G. Clark, P. Rivera, J. S. Ross, K. L. Seyler, W. Yao, and X. Xu, *Nat. Rev. Mater.* **1**, 16055 (2016).
- [6] K. Takashina, Y. Ono, A. Fujiwara, Y. Takahashi, and Y. Hirayama, *Phys. Rev. Lett.* **96**, 236801 (2006).
- [7] Z. Zhu, A. Collaudin, B. Fauqué, W. Kang, and K. Behnia, *Nat. Phys.* **8**, 89 (2012).
- [8] A. Rycerz, J. Tworzydło, and C. W. J. Beenakker, *Nat. Phys.* **3**, 172 (2007).
- [9] D. Gunlycke and C. T. White, *Phys. Rev. Lett.* **106**, 136806 (2011).
- [10] C. Zhao, T. Norden, P. Zhang, P. Zhao, Y. Cheng, F. Sun, J. P. Parry, P. Taheri, J. Wang, and Y. Yang, *Nat. Nanotechnol.* **12**, 757 (2017).
- [11] H. Zeng, J. Dai, W. Yao, D. Xiao, and X. Cui, *Nat. Nanotechnol.* **7**, 490 (2012).
- [12] K. F. Mak, K. He, J. Shan, and T. F. Heinz, *Nat. Nanotechnol.* **7**, 494 (2012).
- [13] T. Norden, C. Zhao, P. Zhang, R. Sabirianov, A. Petrou, and H. Zeng, *Nat. Commun.* **10**, 4163 (2019).
- [14] R. Peng, Y. Ma, S. Zhang, B. Huang, and Y. Dai, *J. Phys. Chem. Lett.* **9**, 3612 (2018).
- [15] C. Mai, A. Barrette, Y. Yu, Y. G. Semenov, K. W. Kim, L. Cao, and K. Gundogdu, *Nano Lett.* **14**, 202 (2014).
- [16] M. K. Mohanta and A. De Sarkar, *Phys. Rev. B* **102**, 125414 (2020).
- [17] E. I. Rashba, *Sov. Phys. Solid State* **2**, 1109 (1960).
- [18] G. Dresselhaus, *Phys. Rev.* **100**, 580 (1955).
- [19] Y. A. Bychkov and E. I. Rashba, *JETP Lett.* **39**, 78 (1984).
- [20] Q. Zhang and U. Schwingenschlöggl, *Phys. Rev. B* **97**, 155415 (2018).
- [21] S. Datta and B. Das, *Appl. Phys. Lett.* **56**, 665 (1990).
- [22] S. Gupta and B. I. Yakobson, *J. Am. Chem. Soc.* **143**, 3503 (2021).
- [23] P. Chuang, S.-C. Ho, L. W. Smith, F. Sfigakis, M. Pepper, C.-H. Chen, J.-C. Fan, J. P. Griffiths, I. Farrer, and H. E. Beere, *Nat. Nanotechnol.* **10**, 35 (2015).
- [24] A. Manchon, H. C. Koo, J. Nitta, S. M. Frolov, and R. A. Duine, *Nat. Mater.* **14**, 871 (2015).
- [25] C. Chappert, A. Fert, and F. N. Van Dau, *Nat. Mater.* **6**, 813 (2007).
- [26] T. Jungwirth, J. Wunderlich, and K. Olejník, *Nat. Mater.* **11**, 382 (2012).
- [27] J. Nitta, T. Akazaki, H. Takayanagi, and T. Enoki, *Phys. Rev. Lett.* **78**, 1335 (1997).
- [28] J. Luo, H. Munekata, F. F. Fang, and P. J. Stiles, *Phys. Rev. B* **41**, 7685 (1990).
- [29] K. Ishizaka, M. S. Bahramy, H. Murakawa, M. Sakano, T. Shimojima, T. Sonobe, K. Koizumi, S. Shin, H. Miyahara, and A. Kimura, *Nat. Mater.* **10**, 521 (2011).
- [30] C. R. Ast, J. Henk, A. Ernst, L. Moreschini, M. C. Falub, D. Pacilé, P. Bruno, K. Kern, and M. Grioni, *Phys. Rev. Lett.* **98**, 186807 (2007).
- [31] A. Kimura, E. E. Krasovskii, R. Nishimura, K. Miyamoto, T. Kadono, K. Kanomaru, E. V. Chulkov, G. Bihlmayer, K.

- Shimada, H. Namatame, and M. Taniguchi, *Phys. Rev. Lett.* **105**, 076804 (2010).
- [32] H. Min, J. E. Hill, N. A. Sinitsyn, B. R. Sahu, L. Kleinman, and A. H. MacDonald, *Phys. Rev. B* **74**, 165310 (2006).
- [33] Y. C. Cheng, Z. Y. Zhu, M. Tahir, and U. Schwingenschlöggl, *Euro Phys. Lett.* **102**, 57001 (2013).
- [34] T. Hu, F. Jia, G. Zhao, J. Wu, A. Stroppa, and W. Ren, *Phys. Rev. B* **97**, 235404 (2018).
- [35] R. Ahammed, N. Jena, A. Rawat, M. K. Mohanta, Dimple, and A. De Sarkar, *J. Phys. Chem. C* **124**, 21250 (2020).
- [36] K. Lee, W. S. Yun, and J. D. Lee, *Phys. Rev. B* **91**, 125420 (2015).
- [37] S. Anand, K. Thekkepat, and U. V. Waghmare, *Nano Lett.* **16**, 126 (2016).
- [38] D. Hazra, N. Tsavdaris, S. Jebari, A. Grimm, F. Blanchet, F. Mercier, E. Blanquet, C. Chapelier, and M. Hofheinz, *Supercond. Sci. Technol.* **29**, 105011 (2016).
- [39] Y. F. Wu, A. B. Yu, L. B. Lei, C. Zhang, T. Wang, Y. H. Ma, Z. Huang, L. X. Chen, Y. S. Liu, C. M. Schneider, G. Mu, H. Xiao, and T. Hu, *Phys. Rev. B* **101**, 174502 (2020).
- [40] A. Chanana and U. V. Waghmare, *Phys. Rev. Lett.* **123**, 037601 (2019).
- [41] P. Hohenberg and W. Kohn, *Phys. Rev.* **136**, B864 (1964).
- [42] W. Kohn and L. J. Sham, *Phys. Rev.* **140**, A1133 (1965).
- [43] G. Kresse and J. Furthmüller, *Phys. Rev. B* **54**, 11169 (1996).
- [44] G. Kresse and J. Hafner, *Phys. Rev. B* **49**, 14251 (1994).
- [45] G. Kresse and J. Furthmüller, *Comput. Mater. Sci.* **6**, 15 (1996).
- [46] G. Kresse and J. Hafner, *Phys. Rev. B* **47**, 558 (1993).
- [47] P. E. Blöchl, *Phys. Rev. B* **50**, 17953 (1994).
- [48] G. Kresse and D. Joubert, *Phys. Rev. B: Condens. Matter Mater. Phys.* **59**, 1758 (1999).
- [49] J. P. Perdew, K. Burke, and M. Ernzerhof, *Phys. Rev. Lett.* **77**, 3865 (1996); **78**, 1396(E) (1997).
- [50] J. D. Pack and H. J. Monkhorst, *Phys. Rev. B* **16**, 1748 (1977).
- [51] S. Baroni, P. Giannozzi, and A. Testa, *Phys. Rev. Lett.* **58**, 1861 (1987).
- [52] X. Gonze, *Phys. Rev. A* **52**, 1096 (1995).
- [53] A. Togo, F. Oba, and I. Tanaka, *Phys. Rev. B* **78**, 134106 (2008).
- [54] U. Herath, P. Tavadze, X. He, E. Bousquet, S. Singh, F. Muñoz, and A. H. Romero, *Comput. Phys. Commun.* **251**, 107080 (2020).
- [55] A. Kormányos, V. Zólyomi, N. D. Drummond, P. Rakyta, G. Burkard, and V. I. Fal'ko, *Phys. Rev. B* **88**, 045416 (2013).
- [56] H. U. Din, M. Idrees, A. Albar, M. Shafiq, I. Ahmad, C. V. Nguyen, and B. Amin, *Phys. Rev. B* **100**, 165425 (2019).
- [57] See Supplemental Material at <http://link.aps.org/supplemental/10.1103/PhysRevB.105.045426> for band structure, phonon spectra and dynamical stability, spin texture, Rashba parameters, charge distribution, electrostatic potential, and variation in band gap with applied biaxial strain in the studied 2D monolayers.
- [58] V. Zólyomi, N. D. Drummond, and V. I. Fal'ko, *Phys. Rev. B* **89**, 205416 (2014).
- [59] S. V. Eremeev, I. A. Nechaev, Y. M. Koroteev, P. M. Echenique, and E. V. Chulkov, *Phys. Rev. Lett.* **108**, 246802 (2012).
- [60] K. Wu, J. Chen, H. Ma, L. Wan, W. Hu, and J. Yang, *Nano Lett.* **21**, 740 (2020).
- [61] S. Singh and A. H. Romero, *Phys. Rev. B* **95**, 165444 (2017).
- [62] S. LaShell, B. A. McDougall, and E. Jensen, *Phys. Rev. Lett.* **77**, 3419 (1996).
- [63] Y. M. Koroteev, G. Bihlmayer, J. E. Gayone, E. V. Chulkov, S. Blügel, P. M. Echenique, and P. Hofmann, *Phys. Rev. Lett.* **93**, 046403 (2004).
- [64] Y. Wang, W. Wei, H. Wang, N. Mao, F. Li, B. Huang, and Y. Dai, *J. Phys. Chem. Lett.* **10**, 7426 (2019).
- [65] W. Tang, E. Sanville, and G. Henkelman, *J. Phys.: Condens. Matter* **21**, 084204 (2009).
- [66] M. Mohr, K. Papagelis, J. Maultzsch, and C. Thomsen, *Phys. Rev. B* **80**, 205410 (2009).
- [67] Q. Zhang, Y. Cheng, L.-Y. Gan, and U. Schwingenschlöggl, *Phys. Rev. B* **88**, 245447 (2013).
- [68] C. E. Nebel, *Nat. Mater.* **12**, 690 (2013).
- [69] S. Singh, C. Espejo, and A. H. Romero, *Phys. Rev. B* **98**, 155309 (2018).
- [70] D. Xiao, M.-C. Chang, and Q. Niu, *Rev. Mod. Phys.* **82**, 1959 (2010).
- [71] D. J. Thouless, M. Kohmoto, M. P. Nightingale, and M. den Nijs, *Phys. Rev. Lett.* **49**, 405 (1982).
- [72] M. Gradhand, D. V. Fedorov, F. Pientka, P. Zahn, I. Mertig, and B. L. Györfy, *J. Phys.: Condens. Matter* **24**, 213202 (2012).
- [73] R. Peng, Z. He, Q. Wu, Y. Dai, B. Huang, and Y. Ma, *Phys. Rev. B* **104**, 174411 (2021).
- [74] H. Hu, W.-Y. Tong, Y.-H. Shen, X. Wan, and C.-G. Duan, *npj Comput. Mater.* **6**, 129 (2020).
- [75] N. Jena, R. A. Dimple, A. Rawat, M. K. Mohanta, and A. De Sarkar, *Phys. Rev. B* **100**, 165413 (2019).
- [76] K. Dou, Y. Ma, R. Peng, W. Du, B. Huang, and Y. Dai, *Appl. Phys. Lett.* **117**, 172405 (2020).
- [77] J. Son, K.-H. Kim, Y. H. Ahn, H.-W. Lee, and J. Lee, *Phys. Rev. Lett.* **123**, 036806 (2019).
- [78] S. Li, W. Wu, X. Feng, S. Guan, W. Feng, Y. Yao, and S. A. Yang, *Phys. Rev. B* **102**, 235435 (2020).
- [79] Z. Song, Z. Li, H. Wang, X. Bai, W. Wang, H. Du, S. Liu, C. Wang, J. Han, and Y. Yang, *Nano Lett.* **17**, 2079 (2017).
- [80] M. K. Mohanta, A. Kishore, and A. De Sarkar, *ACS Appl. Mater. Interfaces* **13**, 40872 (2021).